# *Ab initio* study of the optical absorption and wave-vector-dependent dielectric response of graphite

A. G. Marinopoulos,[1] Lucia Reining,[1] Angel Rubio,[2] and Valerio Olevano[1]
[1]*Laboratoire des Solides Irradiés, UMR 7642 CNRS/CEA, École Polytechnique, F-91128 Palaiseau, France*
[2]*Departamento de Física de Materiales, Facultad de Químicas, Universidad del País Vasco, Centro Mixto CSIC-UPV/EHU and Donostia International Physics Center (DIPC), 20018 San Sebastián/Donostia, Spain*
(Received 15 October 2003; revised manuscript received 29 March 2004; published 30 June 2004)

We performed *ab initio* calculations of the optical absorption spectrum and the wave-vector-dependent dielectric and energy-loss functions of graphite in the framework of the random-phase approximation. In the absorption spectrum, the most prominent peaks were analyzed in terms of interband transitions from specific regions of the Brillouin zone. The inclusion of the crystal local-field effects (LFE) in the response had an important influence on the absorption spectrum for light polarization parallel to the **c** axis. The calculated electron energy-loss spectra, even without LFE, were in very good agreement with existing momentum-dependent energy-loss experiments concerning the peak positions of the two valence-electron plasmons. Important aspects of the line shape and anisotropy of the energy-loss function at large momentum transfer $q$ were also well described: the splitting of the total $(\pi+\sigma)$ plasmon and the appearance of peaks originating from interband transitions. Finally, the role of the interlayer interaction was studied, in particular with regard to its effect on the absorption spectrum for light polarization parallel to **c**, and to the position of the higher-frequency $\pi+\sigma$ plasmon.

DOI: 10.1103/PhysRevB.69.245419 PACS number(s): 81.05.Uw, 71.45.−d, 78.67.−n, 79.20.Uv

## I. INTRODUCTION

Hexagonal graphite is an important technological material with diverse uses, e.g., in catalysis and intercalation applications.[1] It is a layered solid with a rather large $(c/a)_{\mathrm{hex}}$ ratio (approximately 2.73).[2] It consists of an ABA stacking of hexagonal planes of carbon (graphene layers/sheets; see Fig. 1) parallel to the crystallographic **c** axis (an alternative ABC stacking sequence of rhombohedral symmetry is also present in defective graphite[2]). This layered graphene-based structure and the anisotropy in the chemical bonding ($\sigma$ covalent bonds between nearest neighbors in the layer versus weak $\pi$ interlayer coupling) render graphite a very anisotropic solid and a typical example of a quasi-two-dimensional system.[3] Furthermore, other important carbon-based systems contain graphene as a building block. In particular, carbon nanotubes are composed of cylindrically-rolled graphene sheets of various diameters and helicities and their electronic properties were explained (under certain conditions, e.g., neglect of curvature and $\sigma-\pi$ hybridization) in terms of the two-dimensional band structure of graphene.[4] Recently it was also predicted that all laminar materials may form nanotubes[5] and, hence, one may take graphite as representative for a whole class of important layered materials forming nanostructured compounds. All the above facts have renewed the interest for the electronic structure and dielectric properties of graphite and graphene.

From an experimental standpoint, the dielectric response functions of graphite were determined by optical[6,7] spectroscopy (long-wavelegth $\mathbf{q}\rightarrow 0$ limit) as well as electron energy loss (EELS) (Refs. 8–14) and inelastic x-ray scattering[15] spectroscopies as a function of the momentum-transfer vector **q**. In particular, extensive experimental studies by momentum-dependent EELS for **q** oriented parallel to the graphitic basal plane (the $x-y$ plane in Fig. 1), showed that the energy-loss spectra in the valence-energy region (low-loss; up to 50 eV) are dominated by two characteristic plasmon peaks.[10,12] These peaks originate from the collective excitations of the $\pi$ valence electrons ($\pi$ plasmon at 7–12 eV) and of all valence electrons (more intense and broader $\pi+\sigma$ plasmon at 28–33 eV).

Theoretically, the graphitic optical absorption spectrum has been simulated by the joint density of states (JDOS) (Ref. 16) or by parametrized $\pi$-band matrix elements determined in the tight-binding approximation.[17,18] Recently, it was also calculated from first principles, using density functional theory (DFT) in the local density approximation (LDA) to determine the Kohn-Sham electronic structure[19] and the independent-particle response function. **q**-dependent

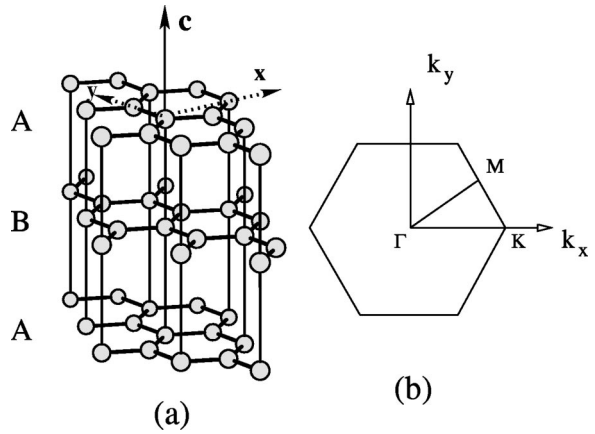


FIG. 1. (a) Graphite; ABA stacking sequence of graphene sheets. (b) Two-dimensional section of the Brillouin zone at the zone center.

 

dielectric and energy-loss functions were also determined from tight-binding model calculations[20] in a frequency range up to 15 eV, i.e., considering explicitly only the interband transitions from occupied $\pi$ electron to unoccupied $\pi^*$ electron states.

Besides the JDOS calculations the above theoretical studies of the dielectric response were based on the random-phase approximation (RPA) where exchange and correlation effects in the response are not considered.[21] Furthermore, the crystalline local-field effects (LFE) which originate from the density variation of the Hartree potential were neglected. The latter effects can be very important for systems such as graphite with significant inhomogeneity in the electronic valence charge density distribution and especially for the $q$-dependent response which should be affected by the microscopic inhomogeneities in the charge density.

In a recent publication[22] we determined the small-$q$-limit graphitic dielectric response functions in the framework of time-dependent density functional theory in both the RPA and also including exchange and correlation effects in the response within the adiabatic LDA (TDLDA).[23,24] Our results for the energy-loss function were in very good agreement with high-resolution EELS measurements[22] for a wide range of **q** orientations. We found that for **q** orientations out of the basal plane the energy-loss spectrum is no longer dominated by two well-defined plasmon peaks: the operation of selection rules at low frequencies and the presence of an electron-hole pair excitation continuum at higher frequencies (18–45 eV) modify the energy-loss line shape. Furthermore, we have shown that LFE in the response become increasingly important for out-of-basal plane **q** orientations whereas exchange and correlation effects turned out to be less important.

In the present work we determine the optical absorption spectra and the **q**-dependent dielectric and energy-loss functions of graphite. The latter are determined as a function of **q** for two nonequivalent in-plane directions on the basal plane for $q$ up to 1.35 $\text{Å}^{-1}$. For this purpose we have carried out RPA calculations with and without LFE. One expects LFE *a priori* to be more important for larger $q$ since an external perturbation of shorter wavelengths will induce microscopic electric fields of the range of the interatomic distances. Therefore, even for in-plane polarizations LFE should be expected to influence the dielectric response at sufficiently large $q$: this tendency was confirmed in a recent TDLDA study[25] of the plasmon dispersion in diamond which is also characterized by highly directional covalent C–C bonds. The validity of RPA to reproduce the plasmon dispersion for a wide range of $q$'s is checked by comparisons with the existing data obtained from $q$-dependent energy-loss experiments.[10,12]

Finally, we also present here a more complete analysis of the effect of the interlayer interaction on the dielectric response. The present results for various interlayer spacings are $q$-dependent and, therefore, complement our previous calculations. This issue merits a particular attention since it yields information about several features of layered systems (including $MgB_2$, cuprate superconductors, chalcogenides[26]) and also of other carbon-based structures, e.g., multiwall nanotubes and bundles of tubes where wall–wall interactions are present.

## II. THEORETICAL FRAMEWORK

As a first step, we determined the electronic ground state of graphite within density functional theory assuming the ABA Bernal stacking sequence of the graphene layers and the experimental lattice parameter $a_{\text{hex}}$ and $(c/a)_{\text{hex}}$ ratio (2.46 Å and 2.73, respectively[2]). The structure is shown in Fig. 1 where the spacing between two adjacent A and B layers (graphene sheets) is equal to half the lattice parameter, $c_{\text{hex}}$, i.e., 3.355 Å. The experimental values for the lattice parameters are reproduced by DFT-LDA pseudopotential calculations[27–29] to within 2%.

In the present work for the valence-core interaction we have used norm-conserving pseudopotentials which were generated from free-atom calculations.[30] The crystalline valence-electron wave functions were expanded using a plane-wave basis set and an energy cutoff of 62 Rydberg. The Kohn-Sham single-particle equations were solved self-consistently in the LDA for exchange and correlation[31] considering 120 **k** points in the irreducible part of the Brillouin zone.

The resulting Kohn-Sham band structure along high-symmetry directions in the first Brillouin zone is shown in Fig. 2 and is very similar to the earlier pseudopotential[27,29] and all-electron[19,32] DFT results. The major features of the band structure are also in a qualitative agreement with the experimental measurements[33] by photoemission[34,35] and very-low energy electron diffraction.[36] Among the quantitative discrepancies we could mention: first, the experimental valence bandwidth determined by photoelectron momentum spectroscopy[37] is 22 eV, i.e., stretched by 11% with respect to the DFT bandwidth. Secondly, photoemission data give the top of the valence $\sigma$ band (at the $\Gamma$ point) at 4–5 eV (with respect to the Fermi energy, $E_F$), whereas the DFT-predicted position is at 3 eV. Self-energy corrections calculated within the GW approximation bring the DFT Kohn-Sham band structure in much better agreement with experiment.[35–38] Of course, Kohn-Sham eigenvalues are not meant to reproduce experimental photoemission data, and these discrepancies do not imply that quantities that can be calculated using an expression involving Kohn-Sham eigenvalues, such as the dielectric function, are ill described.

In Fig. 2 we also denote the $\pi$ or $\sigma$ character of the bands. This will help to explain the origin of the interband transitions yielding peaks in the optical spectrum (to be discussed in the section that follows).

From the resulting eigenvalues and eigenfunctions the linear response independent-particle polarizability $\chi_0$ (Ref. 39) was constructed. The use of the pseudopotential approximation may not be *a priori* justified for the higher-energy conduction states.[40] Nonetheless, the approach of using pseudo-wave-functions for the calculation of matrix elements is well documented for carbon,[41,42] and was found to be justified. One should also note that the 1$s$ core electrons of carbon in graphite have a very high binding energy, equal to 284 eV.[15] Therefore, the core electrons need not be treated explicitly and the valence response functions may be well described by the pseudo-wave-functions.

Within TDLDA, the full polarizability $\chi$ is connected to $\chi_0$ via the Dyson-type expression[21]

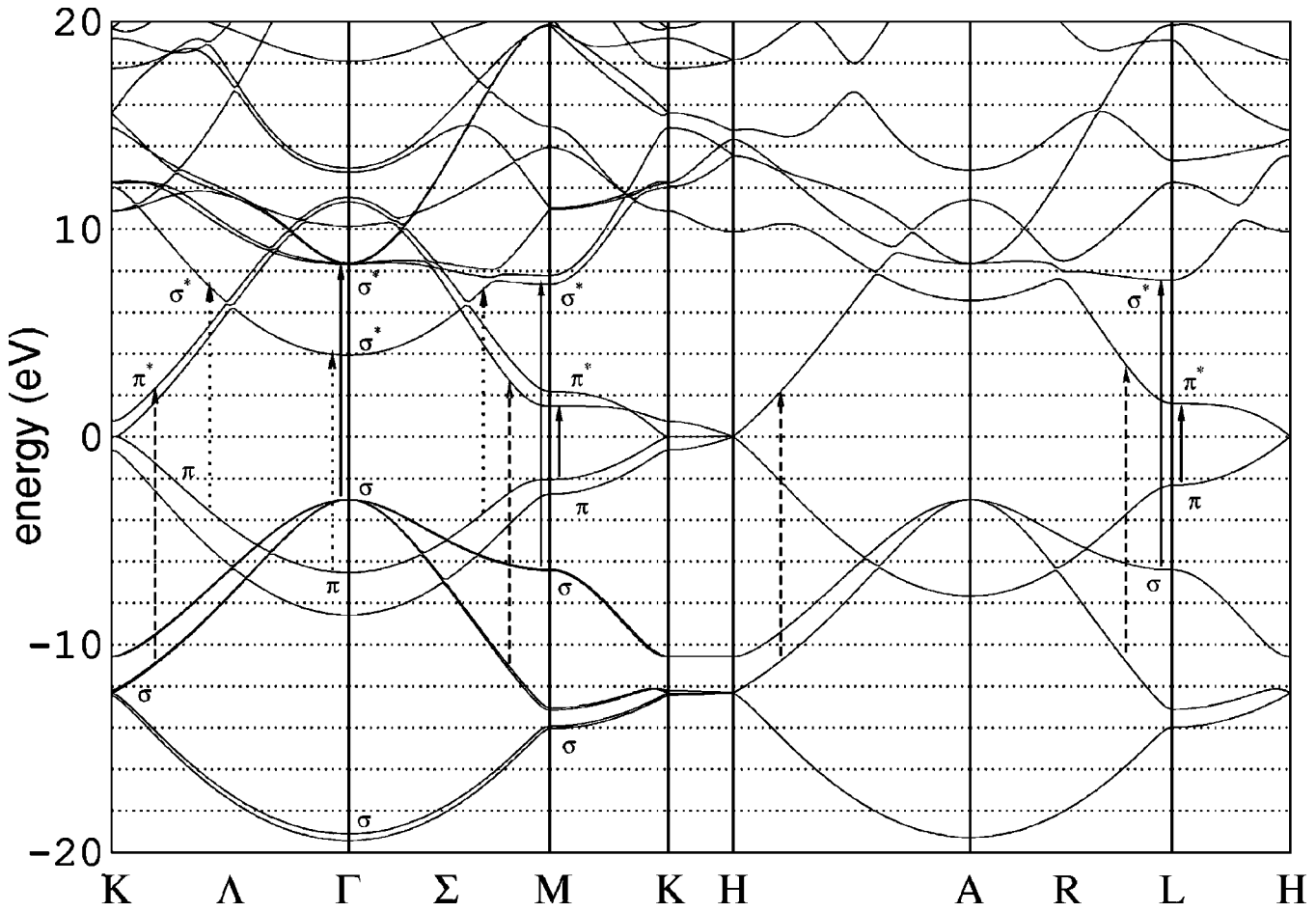


FIG. 2. Kohn-Sham band structure of graphite along high-symmetry directions in the Brillouin zone. Arrows denote interband transitions. The Fermi energy, $E_F$, is taken as the reference energy. ΓK=1.70 Å$^{-1}$ and ΓM=1.47 Å$^{-1}$. Symmetry points A, L, and H define the plane which is parallel to Γ-M-K and passes from the zone edge. Therefore the KH segment is parallel to the **c** axis.

$$\chi = \chi_0 + \chi_0(V_C + f_{\mathrm{xc}})\chi, \tag{1}$$

where $V_C$ is the bare Coulomb interaction and $f_{\mathrm{xc}}$, the so-called exchange-correlation kernel, is the functional derivative of the LDA exchange-correlation potential with respect to the electron density. By setting $f_{\mathrm{xc}}$ to zero, exchange and correlation effects in the electron response are neglected and one obtains the random-phase approximation (RPA) which was used in this work.[43] The inverse longitudinal microscopic dielectric function[39,44] for a periodic system is obtained as:

$$\varepsilon^{-1}_{\mathbf{G},\mathbf{G}'}(\mathbf{q}) = \delta_{\mathbf{G},\mathbf{G}'} + V_C(\mathbf{q}+\mathbf{G})\chi_{\mathbf{G},\mathbf{G}'}(\mathbf{q}) \tag{2}$$

with **q** in the first Brillouin zone and **G**, **G**′ are reciprocal lattice vectors. The energy-loss function for a transferred momentum (**q**+**G**) is given by $-\mathrm{Im}[\varepsilon^{-1}_{\mathbf{G},\mathbf{G}}(\mathbf{q})] = -\mathrm{Im}[V_C(\mathbf{q}+\mathbf{G})\chi_{\mathbf{G},\mathbf{G}}(\mathbf{q})]$. In inhomogeneous systems, e.g., clusters, periodic solids, and structural imperfections the inhomogeneity in the electron response gives rise to LFE and the $\varepsilon_{\mathbf{G},\mathbf{G}'}$ cannot be considered as being purely a diagonal matrix. Therefore, its off-diagonal elements have to be included in the matrix inversion. Making the approximation $\varepsilon^{-1}_{\mathbf{G},\mathbf{G}}(\mathbf{q}) \approx 1/\varepsilon_{\mathbf{G},\mathbf{G}}(\mathbf{q})$ corresponds to neglecting the inhomogeneity of the response, i.e., to neglecting the LFE.

In the sections that follow we shall present our results on the $q$-dependent macroscopic dielectric function $\varepsilon_M$ which is defined as: $\varepsilon_M(\mathbf{q}) = 1/\varepsilon^{-1}_{0,0}(\mathbf{q})$. For the specific case where LFE are neglected: $\varepsilon_M(\mathbf{q}) = \varepsilon_{0,0}(\mathbf{q})$. The optical absorption spectrum is obtained as the imaginary part of $\varepsilon_M(\mathbf{q}\to 0)$. In this long-wavelength limit the vector **q** stands for the transverse polarization vector of the electric field, **E**.[45]

### III. OPTICAL ABSORPTION SPECTRUM ($q\to 0$)

The calculated RPA optical absorption spectra for graphite with and without LFE are shown in Fig. 4(a) for in-plane light polarization ($\mathbf{E}\perp\mathbf{c}$) and in Fig. 5(a) for polarization parallel to the **c** axis ($\mathbf{E}\parallel\mathbf{c}$), where **E** is the electric field vector.

The in-plane spectrum is dominated by two peak structures: the first one covers the low frequency range (up to 5 eV) starting with very intense contributions below 1 eV and ends with a pronounced peak at 4 eV. The second peak structure sets in beyond 10 eV and has a broader frequency range with a pronounced peak at 14 eV. The origin of the

peaks at 4 and 14 eV is due to $\pi \rightarrow \pi^*$ and $\sigma \rightarrow \sigma^*$ interband transitions, respectively, according to the earlier interpretations by Bassani and Parravicini[16] who assumed a two-dimensional approximation (no interaction between the graphene sheets) and the operative dipole selection rules for this polarization. We have verified that this is indeed the case by calculating the oscillator strength for specific transitions between bands in the Brillouin zone. The $\pi \rightarrow \pi^*$ type transitions (between the bands of $\pi$ and $\pi^*$ character close to the Fermi energy $E_F$) are responsible for the peak structure in the spectrum at 0–5 eV. The most prominent peak in this range is at 4 eV and originates from $\pi \rightarrow \pi^*$ transitions between parallel bands in the region of the M and L points of the Brillouin zone (denoted by the solid arrows in Fig. 2).

For the oscillator strength in the spectrum which sets in beyond 10 eV our calculations showed that it originates from $\sigma \rightarrow \sigma^*$ transitions and more specifically the higher-occupied valence $\sigma$ states are mostly involved. In fact, the lower-lying valence $\sigma$ states (i.e., the ones with the more negative energies: all six $\sigma$ states at the K point, the lower two at $\Gamma$ and the lower four at M; see Fig. 2) have a negligible contribution to the absorption spectrum up to 20 eV for this polarization. Consequently, only the remaining higher-filled $\sigma$ valence states contribute to the absorption beyond 11 eV giving rise to the 14 eV peak in the spectrum; these higher-occupied states are the ones at the $\Gamma$ and M points of the Brillouin zone and in between. The corresponding interband transitions occurring at the $\Gamma$ and M points are denoted by the solid arrows in Fig. 2. From the dispersion and also position of the corresponding $\sigma$ and $\sigma^*$ bands at $\Gamma$ and M it can be inferred that the $\sigma \rightarrow \sigma^*$ transitions in the neighborhood of $\Gamma$ (or A) give rise to the threshold of the peak structure whereas the $\sigma \rightarrow \sigma^*$ transitions at the saddle points M (and L) must yield the prominent absorption peak at 14 eV.

LFE are found to be nearly negligible for this polarization. This is not surprising since for in-plane polarizations graphite is rather homogeneous in the long-wavelength limit ($q \rightarrow 0$). The general aspects of the spectrum—peak positions, their intensity and line shape—are in close agreement with the existing experimental results[6,7,9,11,46] and the previous all-electron calculation[19] where LFE were neglected. One discrepancy between the present results and the experiment is the position of the 4 eV peak. The latter is instead observed at 4.6 eV experimentally. This discrepancy might be due to the neglect of exchange and correlation contributions: First, the self-energy corrections[37] for the occupied $\pi$ and unoccupied $\pi^*$ states calculated within the GW approximation amounted to an opening of the gap at the M point of the Brillouin zone: The $\pi$ states shift downwards in energy by 0.5 eV and the $\pi^*$ states shift upwards by 0.3 eV. These corrections would induce a blueshift of the absorption peak towards approximately 4.8 eV. Such a shift coupled with a small possible backshift towards lower frequencies from the electron-hole interaction also neglected here would yield an improved agreement with experiment.

The absorption spectrum of graphite for the light polarization parallel to the **c** axis is shown in Fig. 5(a). It is characterized by a weak intensity in the low frequency range (below 10 eV) and important peaks in the frequency range beyond 10 eV. The origin of these peaks is due to $\pi \rightarrow \sigma^*$ and/or $\sigma \rightarrow \pi^*$ interband transitions according to the selection rule analysis of Bassani and Parravicini.[16] We have found that the 11 eV peak originates principally from $\pi \rightarrow \sigma^*$ transitions involving the higher occupied $\pi$ band and the lowest unoccupied $\sigma^*$ band. Representative $\pi \rightarrow \sigma^*$ transitions of this type are the ones denoted by the dotted arrows in Fig. 2. It can be seen in Fig. 2 that these interband transitions involve states where the bands are nearly parallel in a large portion of the Brillouin zone, in this case, along the K-$\Gamma$-M direction, (although not along H-A-L), therefore, giving rise to an intense peak at 11 eV (spectrum obtained without LFE). Beyond the 11 eV peak there is also considerable oscillator strength in the spectrum; $\sigma \rightarrow \pi^*$ transitions begin also to contribute (shown as dashed arrows in Fig. 2) and they give rise to the 14 eV peak (spectrum with no LFE). On the basis of the obtained bandstructure and the selection rules for dipole-allowed transitions from Ref. 15, we believe that this 14 eV peak should originate principally from $\sigma \rightarrow \pi^*$ transitions between nearly parallel bands in the $\Sigma$-M regions (and R-L) of the Brillouin zone (dashed arrows in Fig. 2).

However, for this light polarization the bandstructure does not play the exclusive role in defining the absorption spectrum. Now LFE are very important. When LFE are not considered the peak positions for this polarization are at 11 and 14 eV as in the earlier DFT-RPA calculation.[19] However, when LFE are included transitions are mixed and the absorption spectrum is appreciably modified. The main effect of local fields is to shift oscillator strength to higher frequencies. They decrease the intensity of the 11 eV peak and are responsible for the appearance of the 16 eV peak in the spectrum. The latter peak is seen in experiments as a shoulder.[7,9,46]

Finally, the nonzero oscillator strength found below 5 eV should be attributed to the inter-layer interaction which is present in the solid.[18] It is also observed experimentally.[7,9,11,46] The dipole selection rules[16] for an isolated graphene sheet (i.e., complete two-dimensionality) lead to vanishing matrix elements and oscillator strength at this frequency range. LFE do not have any influence on the lower part of the spectrum (less than 10 eV).

The existing experimental evidence is not conclusive for the dielectric function in the 11 eV frequency region. The frequency-dependent $\mathrm{Im}[\varepsilon_M]$ obtained from EELS data[9,11,46] displays a very sharp and intense peak at 11 eV. On the other hand, on the basis of optical measurements[7] the observed maximum at this frequency is of considerably smaller intensity. The earlier interpretations,[47] based on semiempirical tight-binding band-structure calculations for an isolated graphene layer, predicted peak structure between 13 and 16.5 eV. It is therefore also important to understand the effect of the interlayer interaction in the optical spectrum and if this interaction is primarily responsible for the occurrence of the intense peak at 11 eV. For this purpose, we progressively increased the inter-layer spacing (doubling and tripling the $(c/a)_{\mathrm{hex}}$ ratio). This yields stackings of graphene layers in the unit cell with much weaker mutual interaction. The Kohn-Sham band structures for the graphene-sheet geometries with the double and triple $(c/a)_{\mathrm{hex}}$ ratios are displayed in Fig. 3. It can be seen now that the valence $\sigma$ and $\pi$

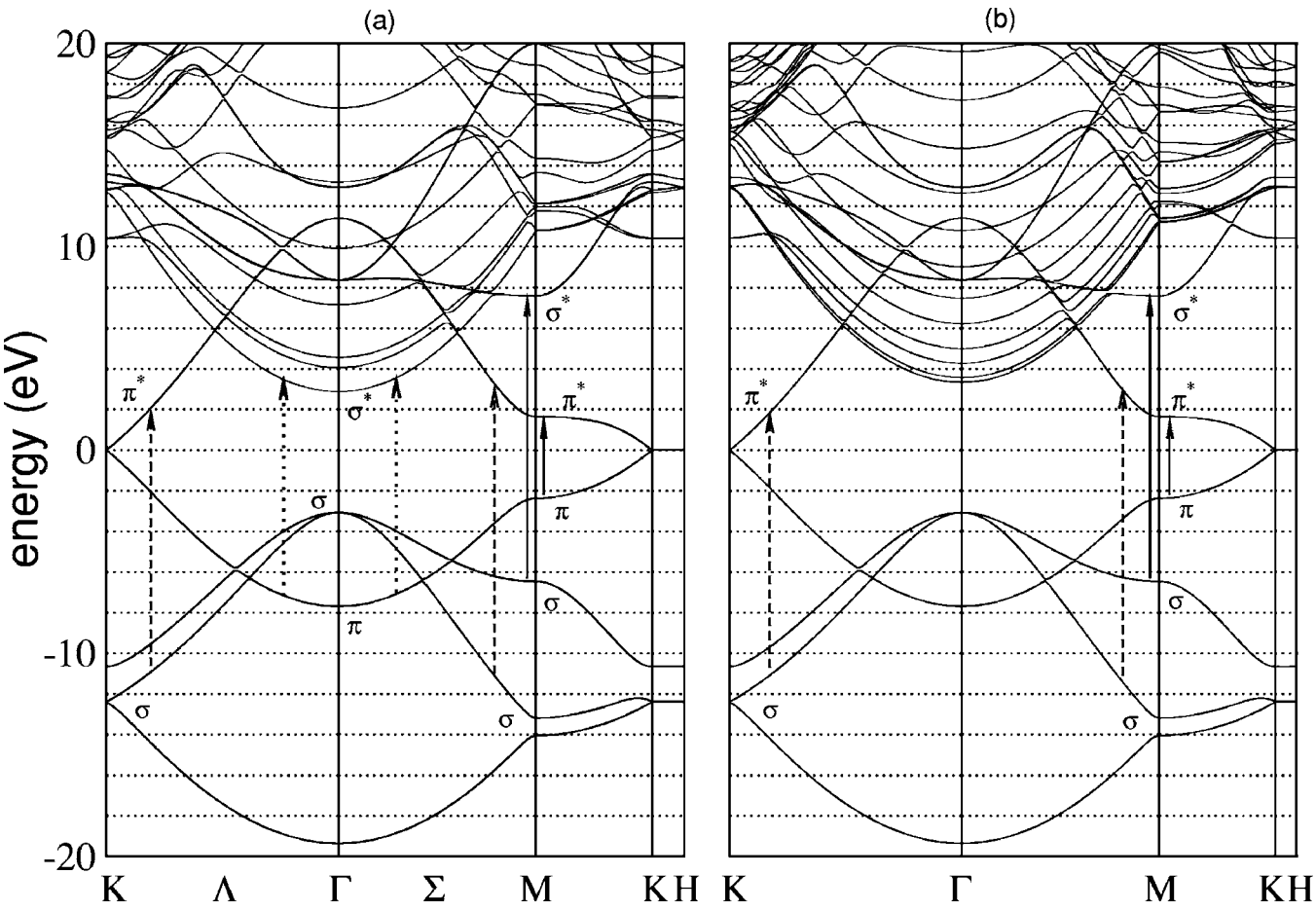


FIG. 3. Kohn-Sham band structure of graphene-sheet geometries with $2(c/a)_{\mathrm{hex}}$ (a), and $3(c/a)_{\mathrm{hex}}$ (b) along high-symmetry directions in the Brillouin zone.

states as well as the $\pi^*$ conduction ones are degenerate along the K-Γ-M direction of the Brillouin zone, i.e., the interlayer interaction is weaker and does not lift the degeneracy as in the case of the solid (Fig. 2). The most important difference between graphite and the graphene geometries is seen in a rather extended region surrounding the Γ point: several unoccupied bands coming most probably from the continuum are now found closer to the Fermi energy in contrast with graphite where only one $\sigma^*$ band exists at 4 eV (measured at Γ) (Fig. 2). This behavior of these conduction bands with increasing $(c/a)_{\mathrm{hex}}$ suggests that they originate from the folding of the Brillouin zone when increasing $(c/a)_{\mathrm{hex}}$ and the periodic boundary conditions applied in the **c**-axis direction. They are folded plane-wavelike states which feel weakly the crystalline potential. In the limit of an isolated graphene layer $[(c/a)_{\mathrm{hex}} \rightarrow \infty]$, they should simply yield a continuum.

Along the **c** axis, i.e., along the KH direction, the dispersion of the valence states is negligible. Nonetheless, certain unoccupied states show a dispersion by 1 eV along KH; this is expected owing to their delocalized nature and can have an effect on the spectra beyond some energy range. For these graphene-sheet geometries we calculated again the optical spectrum for the parallel ($\mathbf{E} \| \mathbf{c}$) polarization.

The first observation [see Fig. 5(b)] is that the oscillator strength vanishes completely in the frequency region below 10 eV in complete accordance with the predictions based on the dipole-selection rules for an isolated graphene layer. Therefore, the double interlayer spacing leads to noninteracting graphene layers as far as the RPA absorption spectrum (in this frequency range) is concerned. When LFE are neglected, the peak structure in the 10–15 eV range stays intact, now with a smaller intensity due to the larger volume. Nonetheless, the spectrum is not uniformly scaled; instead one sees a redistribution of oscillator strength among the 11 and 14 eV peaks. The peak at 11 eV must originate again from the $\pi \rightarrow \sigma^*$ transitions which take place between bands that continue to be parallel in a large portion of the Brillouin zone (dotted arrows in Fig. 3). Similarly, the 14 eV peak from $\sigma \rightarrow \pi^*$ transitions at Σ-M (dashed arrows). With increasing interlayer separation, LFE become progressively more important. For the graphene geometry with $3(c/a)_{\mathrm{hex}}$ the shift of oscillator strength induced by LFE is so big that the absorption peaks in the region 10–15 eV are almost completely suppressed [Fig. 5(c)]. These findings demonstrate that both interlayer interaction and LFE have an important impact on the intensity of the absorption peak at 11 eV.

In conclusion, for parallel polarization in graphite, the theoretically predicted (even with the inclusion of LFE) peak structure remains in qualitative disagreement with experiment. Theory predicts peaks at 11 and 16 eV with a rather

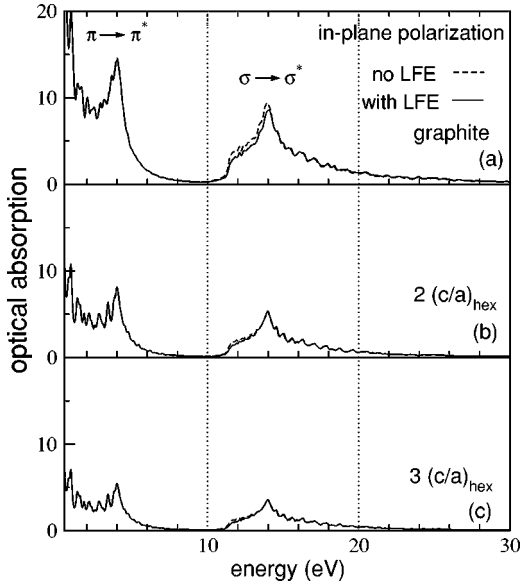


FIG. 4. Optical absorption spectrum of graphite and graphene-sheet geometries with $2(c/a)_{\mathrm{hex}}$ and $3(c/a)_{\mathrm{hex}}$ for $\mathbf{E}\perp\mathbf{c}$. The spectrum is displayed with a broadening of 0.1 eV.

comparable intensity. Experimentally, on the other hand (at least from EELS data), the 11 eV peak is very prominent and the second one at 16 eV appears more like a weak shoulder.[9,11,46] These findings may be taken as an indication that excitonic effects could be present in the experiment. In fact, also in other solids even with a high dielectric constant such as silicon excitonic effects can be significant due to interference effects between transitions involving parallel bands.[48] In such a case, inclusion of excitonic effects would lead to a redistribution of oscillator strength towards lower frequencies increasing the intensity of existing peaks in the spectrum, namely of the first peak here at 11 eV.

Before closing this section it is instructive to also discuss the effect of interlayer interaction for the case of the in-plane polarization. The optical absorption spectra for the graphene sheets (with 2 and $3(c/a)_{\mathrm{hex}}$) are displayed in Figs. 4(b) and 4(c). It can be seen that the spectra decrease in intensity (due to the larger unit-cell volumes) in a uniform manner. They continue to have very similar line shapes with the spectrum of graphite and the two peak positions are again at 4 and 14 eV. This is not surprising since LFE are negligible (no mixing of transitions takes place) and the Kohn-Sham eigenvalues and dispersions of the valence bands and the lower conduction bands at the M point are very similar between graphite and the two graphene-sheet geometries. Therefore the direct $\pi\rightarrow\pi^*$ and $\sigma\rightarrow\sigma^*$ interband transitions which take place in the region of the M point (solid arrows in Figs. 2 and 3) will yield peaks in the optical spectra at 4 and 14 eV, respectively, for both graphite and the graphene geometries.

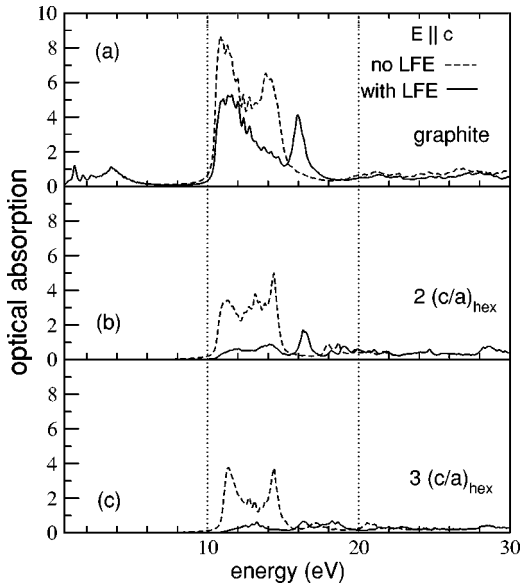


FIG. 5. Optical absorption spectrum for $\mathbf{E}\|\mathbf{c}$, for graphite and the graphene-sheet geometries with $2(c/a)_{\mathrm{hex}}$ and $3(c/a)_{\mathrm{hex}}$.

## IV. *q*-DEPENDENT DIELECTRIC RESPONSE

### A. Evolution of the in-plane response

We have determined the evolution of the graphitic energy-loss function with increasing magnitude of the momentum transfer $\mathbf{q}$. The calculations were done for momentum orientations $\mathbf{q}_x$ and $\mathbf{q}_y$ parallel to two nonequivalent in-plane directions $\mathbf{k}_x$ and $\mathbf{k}_y$, respectively (see Fig. 1). The results are plotted in Figs. 6 and 8 together with the available experimental data.[10,12] The real, $\mathrm{Re}[\varepsilon_M]$, and imaginary, $\mathrm{Im}[\varepsilon_M]$, parts of the $q$-dependent longitudinal dielectric function are also presented in Figs. 7 and 9. The real part gives the screening whereas the imaginary part is a measure of the interband transitions.

For $\mathbf{q}\rightarrow 0$ the energy-loss function is dominated by the two valence-electron plasmons, the $\pi$ and the higher-energy $\pi+\sigma$, which appear as distinct peaks at approximately 7 eV and 28 eV, respectively (Fig. 6). These plasmons represent collective excitations of the $\pi$ and all valence electrons, respectively and their peak positions are very close to the frequencies where $\mathrm{Re}[\varepsilon_M]$ is zero and $\mathrm{Im}[\varepsilon_M]$ becomes very small. These two conditions for $\varepsilon_M$ represent the plasmon existence criterion.[49] The magnitude of $\mathrm{Im}[\varepsilon_M]$ at the frequency where $\mathrm{Re}[\varepsilon_M]$ is zero provides a measure of the plasmon damping due to the electronic interband transitions.[44] This damping causes an increase in the plasmon width and additionally the plasmon peak position in the energy-loss function may not coincide with the zero of $\mathrm{Re}[\varepsilon_M]$.[44] For sufficiently large damping the plasmon resonance will not be an independent excitation mode and may overlap with and/or be immersed into an electron-hole pair excitation continuum.

It can be seen in Figs. 6 and 7 that for small magnitude of $q$ the energies (positions) of both plasmon peaks in the energy-loss function are reasonably close to the positions of the zeroes of the $\mathrm{Re}[\varepsilon_M]$. Nonetheless, even in the $\mathbf{q}\rightarrow 0$ case both plasmons sustain a small degree of damping since $\mathrm{Im}[\varepsilon_M]$ takes finite values close to the plasmon energies. This is in contrast to the case of the homogeneous electron gas where a finite $q$ is needed for the onset of the electron-hole pair excitation region.

Another important observation is that the $\pi$-plasmon position at 7 eV is not solely dictated by excitations of the $\pi$

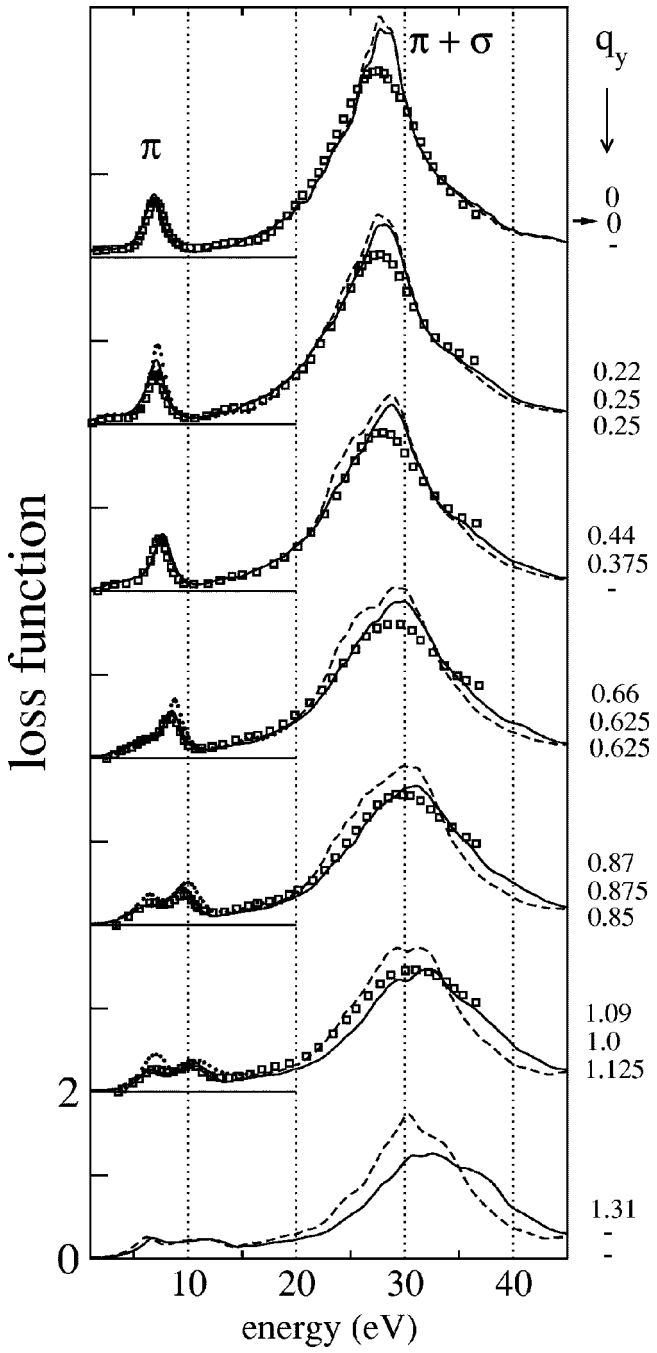


FIG. 6. Momentum-dependent ($q_y$) energy-loss function. Solid (dashed) curves denote present results obtained with (without) LFE. A broadening of 0.5 eV was used here and also for all the response functions in the figures that follow. Experimental data are shown as squares (Ref. 12) and dots (Ref. 10). The magnitude of $q_y$ (in units of $\text{Å}^{-1}$) is given at the right side of the curves: upper is theory, middle is for Ref. 12 and lower for Ref. 10.

electrons (which take place in the 0–5 eV range). In fact, assuming one $\pi$ electron per carbon atom, the electron-gas expression for the $\pi$ plasmon, $\omega_{eg}=(4\pi n_\pi e^2/m)^{1/2}$, would yield a plasmon energy of 12.5 eV, namely largely overestimating the observed energy for this plasmon. This disagreement may be explained as follows: excitations of the deeper lying $\sigma$ electrons start to take place beyond 10 eV, giving

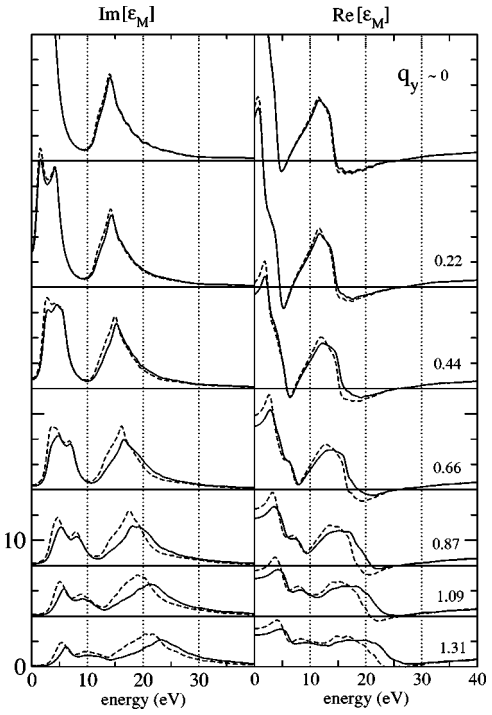


FIG. 7. $q_y$-dependent dielectric function, $\varepsilon_M$. The horizontal axes denote always the zero position. The magnitude of $q_y$ (in units of $\text{Å}^{-1}$) is given at the right side of the curves. Solid (dashed) curves denote results with (without) LFE.

rise eventually to the prominent 14 eV peak in $\text{Im}[\varepsilon_M]$ (Fig. 4). These $\sigma\rightarrow\sigma^*$ transitions cause an abrupt increase of $\text{Re}[\varepsilon_M]$ with frequency (i.e., enhance screening; see Fig. 7) and therefore the zero of $\text{Re}[\varepsilon_M]$ takes place rather fast yielding the occurrence of the $\pi$ plasmon at 7 eV. This is the reason that the $\pi$ plasmon is energetically found very close to the frequency range 0–5 eV of the $\pi\rightarrow\pi^*$ interband transitions. The situation is different for the higher-lying $\pi+\sigma$ plasmon with its peak at 28 eV considerably displaced from the 14 eV peak of the $\sigma\rightarrow\sigma^*$ transitions.

With increasing magnitude of $q$, $\text{Im}[\varepsilon_M]$ undergoes important changes in its line shape. The main trend is a progressive shift of oscillator strength to higher energies with increasing $q$. This behavior is accompanied by a weakening of the electron screening as evidenced by the reduced magnitude of $\text{Re}[\varepsilon_M]$. These observed changes of $\varepsilon_M(\mathbf{q})$ as a function of $q$ have important consequences on the energy-loss function and the plasmon dispersion. With increasing $q$, the frequencies of both valence plasmons increase as well as their effective width, and their line shape undergoes important changes.

Furthermore for large $q$, the plasmon peak positions are found further away from the energy where $\text{Re}[\varepsilon_M]\rightarrow 0$ and the difference between these two energies increases with $q$. These effects are a consequence of damping coming from the interband transitions: $\text{Im}[\varepsilon_M]$ increases (with increasing $q$) in the energy range where the zero of $\text{Re}[\varepsilon_M]$ is located causing also an increase of the $\pi+\sigma$ plasmon width. The $\pi$ plasmon, on the other hand, decays relatively faster with increasing $q$ owing to its weaker intensity and its closer proximity with

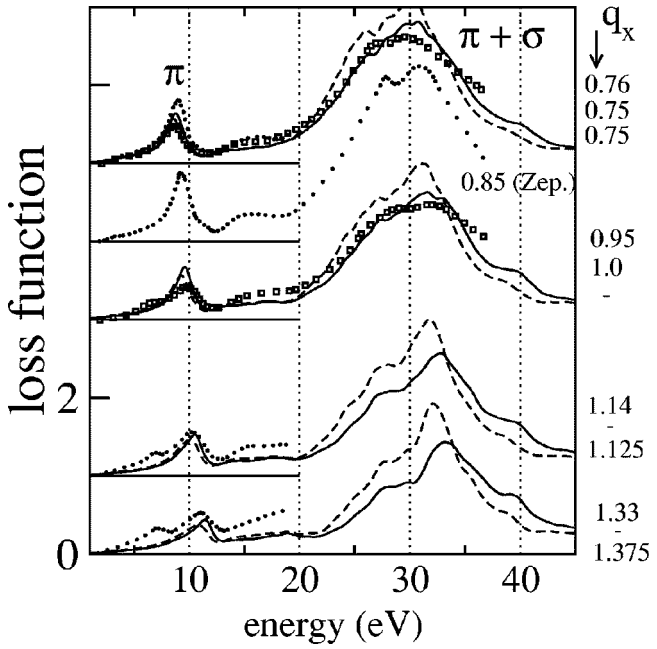


FIG. 8. Momentum-dependent ($q_x$) energy-loss function. The meaning of curves and symbols is the same as in Fig. 6. Zeppenfeld's result (Ref. 10) for $q_x=0.85$ Å$^{-1}$ is explicitly denoted.

the very strong interband transitions present in the 0–5 eV region. Eventually, beyond a certain wave vector $q_c$ close to 1.0 Å$^{-1}$ and for $\mathbf{q}\|\mathbf{k}_y$ the $\pi$ plasmon ceases to exist as a distinct peak in the energy-loss function. Instead, a bimodal diffuse structure of low intensity develops in the energy range 6–14 eV (see Fig. 6).

### B. Anisotropy and local-field effects (LFE)

Anisotropy and LFE manifest themselves in the in-plane dielectric response functions especially for large $q$'s. For small magnitudes of $q$, the most visible effect of local fields is to decrease the real part of $\varepsilon_M$ (i.e., the screening) in the static limit ($\omega=0$). This behavior also persists up to the largest magnitude of $\mathbf{q}$ and for both $\mathbf{q}$ orientations studied here (see Figs. 7 and 9).

For the two different in-plane $\mathbf{q}$ orientations ($\mathbf{q}_x$ versus $\mathbf{q}_y$) the plasmon line shapes and dispersion are very similar for small $q$ values. Also LFE do not play any important role. For magnitudes of $q$ greater than 0.5 Å$^{-1}$, which corresponds to external perturbation of short wavelengths, anisotropy effects are starting to become more important in the dielectric (see Fig. 7 and 9) and energy-loss functions (see Figs. 6 and 8). In the range of lower energies, the energy-loss function for the $\mathbf{q}_y$-orientation develops additional structure in the frequency region 5–10 eV, and at the same time the energy-loss structure decreases in intensity. As a result, a wide-width feature with a bimodal shape appears at the energy range from 5 to 14 eV and the $\pi$ plasmon ceases to exist as a distinct peak in the energy-loss spectrum for $\mathbf{q}\|\mathbf{k}_y$ (see Fig. 6). In contrast, in the same range of energies and $q$'s (and up to 1.3 Å$^{-1}$) the energy-loss function for $\mathbf{q}\|\mathbf{k}_x$ has only one distinct peak (see Fig. 8).

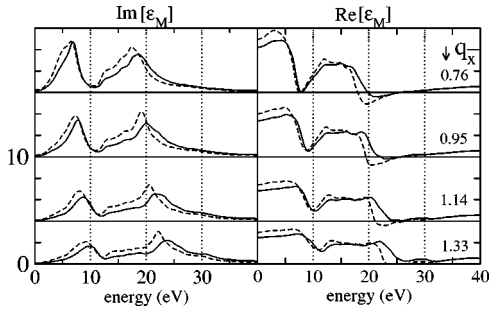


FIG. 9. $q_x$-dependent dielectric function, $\varepsilon_M$. The horizontal axes denote always the zero position. The magnitude of $q_x$ (in units of Å$^{-1}$) is given at the right side of the curves. Solid (dashed) curves denote results with (without) LFE.

The above discussed different line shape in the energy-loss function for the range of energies 5–14 eV is connected with the anisotropic behavior of Im[$\varepsilon_M$] for larger $q$'s. Namely, for $\mathbf{q}\|\mathbf{k}_y$, Im[$\varepsilon_M$] has a double peak structure for energies below 10 eV ($q_y=0.66$, 0.87, and 1.09 Å$^{-1}$ in Fig. 7). Eventually for large $q(>1$ Å$^{-1})$ there is a peak in Im[$\varepsilon_M$] in the range 5–6 eV (see Fig. 7). Such a peak is absent for the case of $\mathbf{q}\|\mathbf{k}_x$ at these large $q$ values (Fig. 9). Its presence signifies the existence of an important decay channel provided by the onset of interband transitions at these energies. This decay mechanism is responsible for the bi-modal feature in the energy-loss function for $\mathbf{q}\|\mathbf{k}_y$ and suggests that the first of the two peak structures in this part of the energy-loss function is not a collective mode (plasmon); instead it reflects the interband transitions seen in Im[$\varepsilon_M$].

Furthermore, inspection of the zero crossings of Re[$\varepsilon_M$] of the raw data (without the artificial 0.5 eV broadening) in the frequency range 5–15 eV showed that Re[$\varepsilon_M$] does not vanish for the large $q$ values of $q_y$ equal to 1.09 and 1.31 Å$^{-1}$ and for $q_x$ equal to 1.33 Å$^{-1}$. Therefore, the observed peaks in the energy-loss function at frequencies 5–15 eV for these large-$q$ magnitudes are not of collective character and cannot be identified as plasmons. These peaks are, again, interband transitions also seen in the Im[$\varepsilon_M$] curves. However, later we shall include these peaks in the plotted plasmon peak positions (Fig. 10) only for the sake of comparison with the peaks observed in the experimental energy-loss measurements.

In the range of higher energies, a shoulder starts to appear with increasing $q$ at the lower-energy side of the $\pi+\sigma$ plasmon for $\mathbf{q}\|\mathbf{k}_x$ and as a result the overall line shape of the plasmon structure is more asymmetric for this momentum orientation (Fig. 8).

For large $q$'s also LFE become very important: they cause an oscillator strength shift to higher frequencies in the Im[$\varepsilon_M$] curves. In the energy-loss function they are far more significant for high energies (beyond 20 eV; as in diamond[25]) and their main effect is to yield changes in the line shape of the total $\pi+\sigma$ plasmon providing additional damping. It can be seen that they cause a shift of the peak of the $\pi+\sigma$ plasmon to higher frequencies and they yield a larger effective plasmon width for larger $q$'s. This larger effective width originates from the oscillator-strength shift to the frequencies

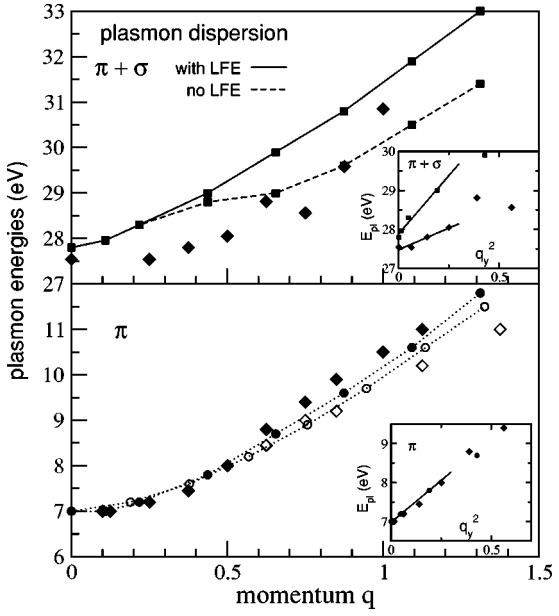


FIG. 10. Plasmon dispersion in graphite. (For large $q$'s some of the peaks represent interband transitions; see text for discussion). Filled (open) symbols denote plasmon-peak positions for in-plane momentum $q_y(q_x)$. The results of our calculations are denoted by squares and circles joined by lines to guide the eye, whereas the diamonds are the experimental data for the $\pi$ (Ref. 10) and $\pi+\sigma$ (Ref. 12) plasmons. $q$ is given in units of $\text{Å}^{-1}$. For the $\pi$ plasmon only the results without LFE are presented. Insets display plasmon-peak energies versus $q_y^2$ and the least-squares-fit lines. The symbols retain their meaning.

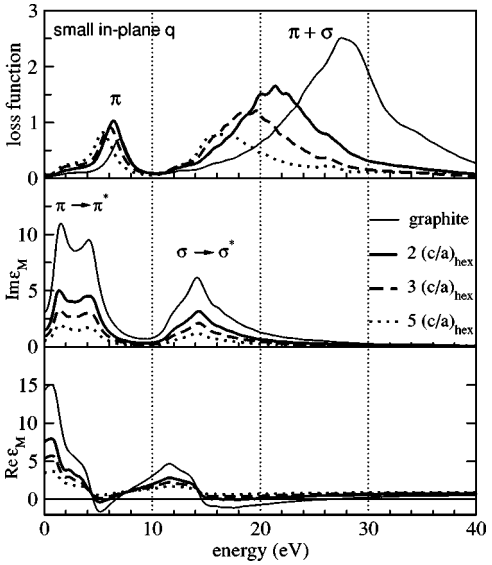


FIG. 11. Energy-loss and dielectric function for small in-plane $q(q_y=0.22\ \text{Å}^{-1})$ for graphite and the graphene-sheet geometries with multiple $(c/a)_{\text{hex}}$ ratios. Only the results without LFE are presented since LFE are negligible in this $q$ range.

where $\text{Re}[\varepsilon_M]$ has a zero, i.e., increasing the damping.

Overall, the calculated in-plane dispersion of the peaks in the energy-loss function—their positions and widths—starting from the optical limit up to a magnitude of $q$ equal to approximately $1.3\ \text{Å}^{-1}$ captures very well the results of the earlier momentum-dependent energy-loss experiments in transmission[10,12] (Figs. 6 and 8). The calculated and experimentally-observed peak positions as a function of momentum $\mathbf{q}$ are displayed in Fig. 10. The agreement between theory and experiment is very good given the difficulty in assigning a peak position, especially for the very wide and asymmetrical $\pi+\sigma$ plasmon. The fact that LFE turn out not to be crucial in the plasmon dispersion is in contrast to the situation studied in our earlier work[22] which dealt with $\mathbf{q}$ orientations out of the basal planes where LFE were very important.

Furthermore, the present RPA calculations correctly reproduce the experimentally observed anisotropic behavior of the $\pi$ plasmons and low-energy peaks in the energy-loss function for $q$'s beyond $0.6\ \text{Å}^{-1}$: namely, the peak energies are higher for the case when $\mathbf{q}\|\mathbf{k}_y$ (see Fig. 10). Also the eventual decay of the $\pi$ plasmon and the ensuing bimodal structure in the energy region from 5 to 14 eV are seen in the experiments for $\mathbf{q}\|\mathbf{k}_y$. For higher energies, and for large $q$'s the calculations also reproduce the observed splitting of the $\pi+\sigma$ plasmon into a double-peaked structure for $\mathbf{q}\|\mathbf{k}_x$ (see Fig. 8), something which is especially evident in the measurement of Zeppenfeld[10] for $q_x=0.85\ \text{Å}^{-1}$.

The fact that the calculated and experimentally-observed energy-loss functions are compared at slightly different $q$-values does not affect our conclusions. Especially for small magnitudes of $q$ (less than $0.5\ \text{Å}^{-1}$), the plasmon dispersion is very limited (Fig. 6) and, therefore, $\mathbf{q}$ vectors differing in modulus by 0.03 or $0.065\ \text{Å}^{-1}$ will not lead to any noticeable changes in the energy-loss function.[50]

The most significant difference between the present calculations and experiment shows up for larger $q$'s in the energy region 14–20 eV of the continuum: for $\mathbf{q}\|\mathbf{k}_x$ the experimental electron-hole pair excitation continuum displays a rather large intensity in contrast to our results which show a flat line shape of small intensity (see Fig. 8). Furthermore, a shoulder at 7 eV (for $q_x>1\ \text{Å}^{-1}$) is not obtained from the calculations. Both new experimental verification (note also that Zeppenfeld's measurements display an increased intensity for the peak structure at 7 eV with respect to Büchner's for $\mathbf{q}\|\mathbf{k}_y$) and an estimate of exchange and correlation effects in the theory would be necessary to clarify these points.

We would also like to discuss, at this point, the plasmon dispersion in the small-$q$ limit, which is predicted to be quadratic in $q$ for the case of the interacting electron gas (see, e.g., Ref. 44), namely, $E_{\text{pl}}(\mathbf{q})=E_{\text{pl}}(0)+\alpha\,\hbar^2/m\,q^2$, where $E_{\text{pl}}(\mathbf{q})$ is the $q$-dependent plasmon energy and $\alpha$ the dispersion coefficient. Our calculations show that the $\pi$-plasmon energy displays a quadratic dependence on $q$, for small $q$ values (see inset of Fig. 10). This has also been recognized in the past for the experimentally observed $\pi$-plasmon peaks,[51,52] which are well reproduced from the present calculations and with a well-defined coefficient $\alpha$. Nonetheless, no definitive conclusion can be drawn for the $\pi+\sigma$ plasmon in this regard. Although an approximately quadratic dependence on $q$ can be inferred for both calculated and experimental peak positions (see inset of Fig. 10), the value of $\alpha$ is obtained with a very high uncertainty. The reason (which

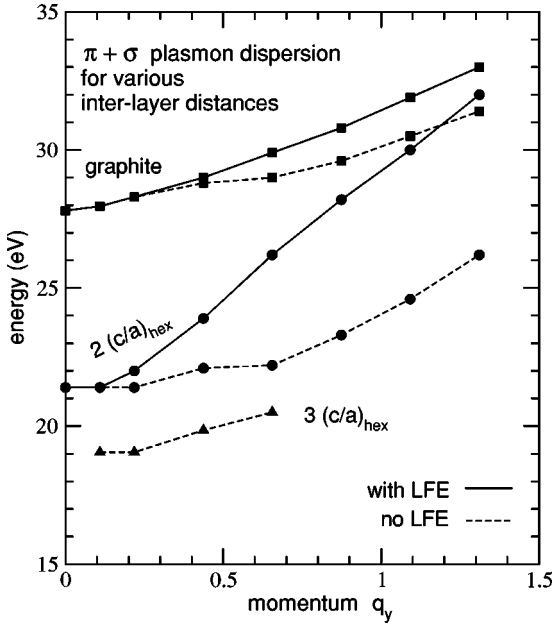


FIG. 12. Dispersion of the $\pi+\sigma$ plasmon for graphite and graphene-sheet geometries with multiple $(c/a)_{\mathrm{hex}}$ ratios. Solid (dashed) curves connect peak positions obtained with (without) LFE. The in-plane momentum $q_y$ has units of $\text{Å}^{-1}$.

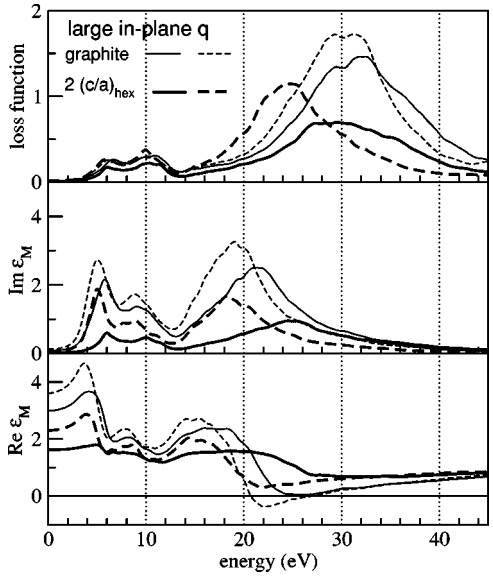


FIG. 13. Energy-loss and dielectric function for large in-plane $q(q_y=1.09\ \text{Å}^{-1})$ for graphite and the graphene-sheet geometry with $2(c/a)_{\mathrm{hex}}$ (thicker curves). Solid (dashed) curves denote results with (without) LFE.

concerns both calculation and experiment) is due to the fact that there exists a very significant uncertainty in defining the $\pi+\sigma$ plasmon position, owing to the asymmetry and the skew shape of the plasmon. For instance, for $q_y=0.44\ \text{Å}^{-1}$ the center of gravity of the calculated plasmon does not coincide with the position of the peak; they differ by approximately 0.8 eV.

The plasmon line shape and energy is affected by the interband transitions and the background polarization. In particular, an estimate of the shift of the plasmon energy with respect to its predicted value, $\omega_{eg}$, for an electron gas of the same average electron density (the electron-gas energy is 25 eV for the $\pi+\sigma$ plasmon) can be provided by the expression[52]

$$\omega_{\mathrm{pl}}^2=\frac{\omega_{eg}^2+\omega_n^2}{1+\chi_b}, \tag{3}$$

where $\chi_b$ is the polarizability of the electrons of more deeply bound shells and $\omega_n$ the eigenfrequency of the electrons participating in the plasmon oscillation. Expression (3) for the case of the $\pi+\sigma$ plasmon, can be evaluated by taking a vanishing $\chi_b$, and substituting the calculated peak frequency of the $\sigma\rightarrow\sigma^*$ interband transitions (equal to 14 eV) for $\omega_n$. The resulting plasmon energy $\omega_{\mathrm{pl}}$ is found to be 28.7 eV, in very good agreement with the calculated energy (28 eV) in the $q\rightarrow 0$ limit (Fig. 10).

For the case of the $\pi$ plasmon, the large decrease of the electron-gas value of its energy (12.5 eV) to 7 eV can be understood by taking $\omega_n$ equal to 4 eV (the prominent peak due to the $\pi\rightarrow\pi^*$ transitions) and by assuming a background polarizability $\chi_b$ (due to the screening from the $\sigma$ electrons) equal to 2.5.

### C. Effect of interlayer interaction

In order to understand how the interlayer interaction affects the graphitic dielectric response we have made a series of calculations (beyond the ones reported in Ref. 22) for a number of graphene-sheet geometries obtained by increasing the layer–layer separation, therefore, effectively increasing $(c/a)_{\mathrm{hex}}$ and the unit-cell volume.

Our results for the dielectric and energy-loss functions for small in-plane **q** are displayed in Fig. 11. Since LFE were found negligible in this case only the results without LFE are shown. It can be seen from the plotted $\mathrm{Im}[\varepsilon_M]$ that the frequency range of the interband transitions is the same for the solid (graphite) and the graphene-sheet geometries (multiple ratios of $(c/a)_{\mathrm{hex}}$) and the corresponding peak positions in the absorption do not change for different $(c/a)_{\mathrm{hex}}$. Instead, the oscillator strength is consistently decreasing with increasing inter-layer separation in a uniform manner, i.e., it is inversely proportional to the total volume. As discussed earlier, this is due to the fact that the peak positions originate from nearly direct interband transitions (small-$q$ limit) between electron states (at specific regions of the Brillouin zone) whose energies and dispersion are stable with respect to variations of the interlayer distance.

In the energy-loss function, it can be seen that the plasmon peak positions shift to lower frequencies when the interlayer separation is increased. This effect is very pronounced for the $\pi+\sigma$ total plasmon position: the total plasmon is extremely sensitive to the interlayer interaction for small in-plane $q$'s. This can be explained as follows: with increasing $(c/a)_{\mathrm{hex}}$, i.e., interlayer spacing, the macroscopic screening vanishes $(\mathrm{Re}[\varepsilon_M]\rightarrow 1$; see Fig. 11) with the effect that $-\mathrm{Im}[1/\varepsilon_M]\rightarrow\mathrm{Im}[\varepsilon_M]$, namely, a coincidence of the energy-loss and absorption functions. Since for the in-plane polarization the absorption peaks do not change with vari-

able $(c/a)_{\mathrm{hex}}$, then the energy-loss function undergoes important changes, in particular the $\pi+\sigma$ peak. The latter is displaced at a much faster rate to lower frequencies towards the 14 eV peak of the absorption spectrum whereas the $\pi$ plasmon peak is rather insensitive to $(c/a)_{\mathrm{hex}}$ since its frequency is already found very close to the 0–5 eV peak structure of the $\pi \rightarrow \pi^*$ transitions in $\mathrm{Im}[\varepsilon_M]$.

The effect of reduced macroscopic screening with increasing $(c/a)_{\mathrm{hex}}$ on the response functions can also be rationalized in terms of the polarizabilities $\chi_0$ and $\chi$, i.e., unscreened and screened response. The latter two quantities, in the macroscopic limit describe the absorption and energy-loss function, respectively, which in principle should be different (compare upper panels of Figs. 6 and 7). However, for large $(c/a)_{\mathrm{hex}}$ ratios (and the resulting decrease in macroscopic screening) the absorption and energy-loss functions will tend to be more similar (see Fig. 11).

The $q$-dependent results for the total plasmon dispersion are shown in Fig. 12. It is evident that at small and medium $q$'s the total plasmons for the graphene sheets are shifted to lower frequencies with respect to the one in graphite. However, with increasing $q$ the inclusion of LFE for the case of the graphene geometry with 2 $(c/a)_{\mathrm{hex}}$ changes appreciably the plasmon dispersion. Eventually, for magnitudes of $q$ greater than 1 $\mathrm{Å}^{-1}$ the plasmon frequencies in graphite and the graphene geometry almost coincide.

For large in-plane **q**, the energy-loss and dielectric function are shown in Fig. 13. Now LFE are important and contrary to the small-$q$ limit the position of the higher-frequency absorption peaks (when LFE are included) change with increasing $(c/a)_{\mathrm{hex}}$ ratio; the absorption peak is at 25 eV for the graphene geometry with $2(c/a)_{\mathrm{hex}}$ and at 22 eV for graphite. This is clearly a LFE-induced effect since if one considers only the electronic structure (no LFE), the indirect interband transitions would yield a peak at 19 eV in $\mathrm{Im}[\varepsilon_M]$ for both graphite and the graphene geometry. Therefore, according to the earlier explanation, the reduced screening for the case of the graphene geometry now does not shift too much the $\pi+\sigma$ plasmon to lower frequencies when LFE are included.

## V. CONCLUSIONS

We have reported *ab initio* calculations of the optical absorption and the wave-vector-dependent dielectric response of graphite and of a number of graphene-sheet geometries. The calculations were carried out within the RPA including two important aspects of the response: the interlayer interaction and the effects of crystal local fields (LFE). In the absorption spectra both LFE and the interlayer interaction had an important influence for light polarization parallel to the **c** axis. The interband transitions responsible for the most prominent peaks in the spectra were also identified.

For the energy-loss function, our results obtained for an extended range of magnitudes of the in-plane momentum **q** were in very good agreement with existing momentum-dependent energy-loss experiments. Specifically, the dispersion of the two valence graphitic plasmons—peak positions and their evolution—was well reproduced even without LFE. The appearance of peaks due to interband transitions was also discussed. The interlayer interaction had an important effect on the total $(\pi+\sigma)$ plasmon for small in-plane $q$. In general, the redshift of the plasmon peaks when going from graphite to a quasi-two-dimensional graphene geometry is caused by a decrease of the screening and depends on the frequency range of the interband transitions and the magnitude of $q$.

## ACKNOWLEDGMENTS

This work was supported by the EC-RTN program NANOPHASE (Contract No. HPRN-CT-2000-00167). A.R. acknowledges support from the Ecole Polytechnique during a sabbatical leave in 2001 where this work was started and partial support from Spanish MCyT(MAT2001-0946), University of the Basque Country (9/UPV 00206.215-13639/2001) and COMELCAN (HPRN-CT-2000-00128). Computer time was granted by IDRIS (Project No. 544). Helpful discussions with Thomas Pichler are also acknowledged.

[1] See, e.g., M. S. Dresselhaus and G. Dresselhaus, Adv. Phys. **30**, 139 (1981).
[2] Y. X. Zhao and I. L. Spain, Phys. Rev. B **40**, 993 (1989).
[3] J. Gonzalez, F. Guinea, and M. A. H. Vozmediano, Phys. Rev. B **63**, 134421 (2001).
[4] N. Hamada, S. Sawada, and A. Oshiyama, Phys. Rev. Lett. **68**, 1579 (1992).
[5] S. G. Louie, in *The Chemical Physics of Fullerenes*, edited by W. Andreoni (Kluwer, Dordrecht, 1996), p. 419; A. Zettl, Adv. Mater. (Weinheim, Ger.) **8**, 443 (1996), and references therein.
[6] E. A. Taft and H. R. Philipp, Phys. Rev. **138**, A197 (1965).
[7] R. Klucker, M. Skibowski, and W. Steinmann, Phys. Status Solidi B **65**, 703 (1974).
[8] K. Zeppenfeld, Z. Phys. **211**, 391 (1968).
[9] K. Zeppenfeld, thesis, University of Hamburg, 1969; J. Daniels, C. v. Festenberg, H. Raether, and K. Zeppenfeld, Springer Tracts Mod. Phys. **54**, 77 (1970).
[10] K. Zeppenfeld, Z. Phys. **243**, 229 (1971).
[11] H. Venghaus, Phys. Status Solidi B **71**, 609 (1975).
[12] U. Büchner, Phys. Status Solidi B **81**, 227 (1977).
[13] T. Pichler, M. Knupfer, M. S. Golden, J. Fink, A. Rinzler, and R. E. Smalley, Phys. Rev. Lett. **80**, 4729 (1998).
[14] N. Papageorgiou, M. Portail, and J. M. Layet, Surf. Sci. **454–456**, 462 (2000).
[15] W. Schülke, U. Bonse, H. Nagasawa, A. Kaprolat, and A. Berthold, Phys. Rev. B **38**, 2112 (1988).
[16] F. Bassani and G. Pastori Parravicini, Nuovo Cimento A **50**, 95 (1967).
[17] L. G. Johnson and G. Dresselhaus, Phys. Rev. B **7**, 2275 (1973).
[18] A. Grüneis, R. Saito, G. G. Samsonidze, T. Kimura, M. A. Pi-

menta, A. Jorio, A. G. Souza Filho, G. Dresselhaus, and M. S. Dresselhaus, Phys. Rev. B **67**, 165402 (2003).
[19] R. Ahuja, S. Auluck, J. M. Wills, M. Alouani, B. Johansson, and O. Eriksson, Phys. Rev. B **55**, 4999 (1997).
[20] C. S. Huang, M. F. Lin, and D. S. Chuu, Solid State Commun. **103**, 603 (1997); M. F. Lin, C. S. Huang, and D. S. Chuu, Phys. Rev. B **55**, 13961 (1997); F. L. Shyu and M. F. Lin, *ibid.* **62**, 8508 (2000).
[21] G. Onida, L. Reining, and A. Rubio, Rev. Mod. Phys. **74**, 601 (2002).
[22] A. G. Marinopoulos, L. Reining, V. Olevano, A. Rubio, T. Pichler, X. Liu, M. Knupfer, and J. Fink, Phys. Rev. Lett. **89**, 076402 (2002).
[23] E. Runge and E. K. U. Gross, Phys. Rev. Lett. **52**, 997 (1984); E. K. U. Gross and W. Kohn, *ibid.* **55**, 2850 (1985).
[24] M. Petersilka, U. J. Gossmann, and E. K. U. Gross, Phys. Rev. Lett. **76**, 1212 (1996).
[25] S. Waidmann, M. Knupfer, B. Arnold, J. Fink, A. Fleszar, and W. Hanke, Phys. Rev. B **61**, 10149 (2000).
[26] R. Tenne, Adv. Mater. (Weinheim, Ger.) **7**, 965 (1995).
[27] M. C. Schabel and J. L. Martins, Phys. Rev. B **46**, 7185 (1992).
[28] J. C. Charlier, X. Gonze, and J. P. Michenaud, Europhys. Lett. **28**, 403 (1994).
[29] J. C. Charlier, X. Gonze, and J. P. Michenaud, Phys. Rev. B **43**, 4579 (1991).
[30] We used the method by N. Troullier and J. L. Martins, Phys. Rev. B **43**, 1993 (1991). The pseudopotentials were generated for the $2s^2 2p^2$ atomic configuration taking a core radius of 1.46 Bohr for the wave functions.
[31] P. Hohenberg and W. Kohn, Phys. Rev. **136**, B864 (1964); W. Kohn and L. J. Sham, Phys. Rev. **140**, A1133 (1965); J. P. Perdew and A. Zunger, Phys. Rev. B **23**, 5048 (1981).
[32] J. C. Boettger, Phys. Rev. B **55**, 11202 (1997).
[33] It should also be noted that the Kohn-Sham single-particle energies are not meant to be the true quasiparticle energies of the system.
[34] W. Eberhardt, I. T. McGovern, E. W. Plummer, and J. E. Fisher, Phys. Rev. Lett. **44**, 200 (1980); T. Takahashi, H. Tokailin, and T. Sagawa, Phys. Rev. B **32**, 8317 (1985).
[35] V. N. Strocov, A. Charrier, J. M. Themlin, M. Rohlfing, R. Claessen, N. Barrett, J. Avila, J. Sanchez, and M. C. Asensio, Phys. Rev. B **64**, 075105 (2001).
[36] V. N. Strocov, P. Blaha, H. I. Starnberg, M. Rohlfing, R. Claessen, J. M. Debever, and J. M. Themlin, Phys. Rev. B **61**, 4994 (2000).
[37] C. Heske, R. Treusch, F. J. Himpsel, S. Kakar, L. J. Terminello, H. J. Weyer, and E. L. Shirley, Phys. Rev. B **59**, 4680 (1999).
[38] Self-energy corrections to the Kohn-Sham DFT band structure showed deviations up to 2 eV for the valence $\sigma$ states and smaller ones for the $\pi$ states which lie close to the Fermi energy (Ref. 37).
[39] H. Ehrenreich and M. H. Cohen, Phys. Rev. **115**, 786 (1959); S. L. Adler, *ibid.* **126**, 413 (1962); N. Wiser, *ibid.* **129**, 62 (1963).
[40] Different choices of pseudopotentials did not affect the polarizability $\chi_0$ and the spectra. $\chi_0$ is obtained as a summation over many conduction bands and the small changes in the eigenvalues and wavefunctions were unimportant with respect to the difference from the Fermi energy. This was also explored for the cases of Si- (S. Albrecht, Ph.D. thesis, Ecole Polytechnique, 1999) and $Li_2O$. [S. Albrecht *et al.*, Phys. Rev. B **55**, 10278 (1997)].
[41] A. J. Read and R. J. Needs, Phys. Rev. B **44**, 13071 (1991).
[42] B. Arnaud and M. Alouani, Phys. Rev. B **63**, 085208 (2001).
[43] We have used up to 16464 **k**-points for the Brillouin-zone sums, 121 **G**-vectors in the matrices and up to 100 bands in the sums over unoccupied bands for the polarizability. In these sums we also added a small imaginary part of 0.01 eV to the frequency. Our results are fully converged with respect to the Brillouin zone sampling for frequencies above 1 eV. An investigation of low-frequency (infrared) plasmons in the energy-loss spectrum of this semimetal [see P. Laitenberger and R. E. Palmer, Phys. Rev. Lett. **76**, 1952 (1996)] would require an improved treatment of intraband transitions, and is beyond the scope of the present work.
[44] D. Pines, *Elementary Excitations in Solids* (Benjamin, New York, 1964).
[45] R. Del Sole and E. Fiorino, Solid State Commun. **38**, 169 (1981).
[46] E. Tosatti and F. Bassani, Nuovo Cimento B **65**, 161 (1970).
[47] D. L. Greenaway, G. Harbeke, F. Bassani, and E. Tosatti, Phys. Rev. **178**, 1340 (1969); G. S. Painter and D. E. Ellis, Phys. Rev. B **1**, 4747 (1970).
[48] W. Hanke and L. J. Sham, Phys. Rev. B **21**, 4656 (1980); M. del Castillo-Mussot and L. J. Sham, *ibid.* **31**, 2092 (1985).
[49] See, e.g., W. Jones and N. H. March, *Theoretical Solid State Physics* (Wiley–Interscience, New York, 1973), Vol. 1.
[50] The use of finer **k**-point meshes would allow us to have a larger availability of **q** vectors and, consequently, a closer correspondence with the **q** vectors studied experimentally. For a few representative cases where we did calculate the dielectric functions on a finer mesh, we obtained very similar line shapes.
[51] H. Venghaus, Phys. Status Solidi B **66**, 145 (1974).
[52] H. Raether, *Excitation of Plasmons and Interband Transitions by Electrons*, Springer Tracts in Modern Physics (Springer, Berlin, Heidelberg, 1980), Vol. 88.